remote sensing

MDPI

Article

Estimating All-Weather Surface Longwave Radiation from Satellite Passive Microwave Data

Zhonghu Jiao

State Key Laboratory of Earthquake Dynamics, Institute of Geology, China Earthquake Administration, Beijing 100029, China; jzh@ies.ac.cn

Abstract: Surface longwave radiation (SLR) is an essential geophysical parameter of Earth's energy balance, and its estimation based on thermal infrared (TIR) remote sensing data has been extensively studied. However, it is difficult to estimate cloudy SLR from TIR measurements. Satellite passive microwave (PMW) radiometers measure microwave radiation under the clouds and therefore can estimate SLR in all weather conditions. We constructed SLR retrieval models using brightness temperature (BT) data from an Advanced Microwave Scanning Radiometer 2 (AMSR2) based on a neural network (NN) algorithm. SLR from the European Centre for Medium-Range Weather Forecasts Reanalysis v5 (ERA5) product was used as the reference. NN-based models were able to reproduce well the spatial variability of SLR from ERA5 at the global scale. Validations indicate a reasonably good performance was found for land sites, with a bias of 1.32 W/m^2, root mean squared error (RMSE) of 35.37 W/m^2, and coefficient of determination (R^2) of 0.89 for AMSR2 surface upward longwave radiation (SULR) data, and a bias of −2.26 W/m^2, RMSE of 32.94 W/m^2, and R^2 of 0.82 for AMSR2 surface downward longwave radiation (SDLR) data. AMSR2 SULR and SDLR retrieval accuracies were higher for oceanic sites, with biases of −2.98 and −4.04 W/m^2, RMSEs of 6.50 and 13.42 W/m^2, and R^2 values of 0.83 and 0.66, respectively. This study provides a solid foundation for the development of a PMW SLR retrieval model applicable at the global scale to generate long-term continuous SLR products using multi-year satellite PMW data and for future research with a higher spatiotemporal resolution.

Keywords: surface downward longwave radiation; surface upward longwave radiation; neural network-based model; surface radiation budget; AMSR2; passive microwave remote sensing

Citation: Jiao, Z. Estimating All-Weather Surface Longwave Radiation from Satellite Passive Microwave Data. *Remote Sens.* **2022**, *14*, 5960. https://doi.org/10.3390/rs14235960

Academic Editor: Ralph R. Ferraro

Received: 14 October 2022
Accepted: 21 November 2022
Published: 25 November 2022

1. Introduction

Surface longwave radiation (SLR) is a key parameter for understanding the surface energy balance and global warming [1,2]. Anthropogenic disturbances to the climate, such as greenhouse gas emissions, have caused a gradual increase in downward atmospheric thermal radiation of ~2 W/m^2 per decade [3], resulting in global warming. Cloud longwave radiative feedback in atmospheric circulation is the important modulating mechanism that affects the El Niño−Southern Oscillation [4]. Therefore, long-term global surface radiation budget products contribute to the understanding of climate change and hydrological cycle mechanisms. Currently, SLR derived from thermal infrared (TIR) remote sensing observations is one of the primary ways to estimate global longwave radiation variation [5,6]. TIR remote sensing has been used to retrieve the SLR with a moderate spatial resolution (e.g., 1 km) and good accuracy. However, TIR observations are affected by the water vapor absorption in the atmosphere and cannot penetrate through clouds like other optical wavelengths, hence it cannot perform all-weather SLR estimation. Global average cloud cover is ~67% and plays an important role in the surface radiation budget [7,8]. SLR, especially surface upward longwave radiation (SULR), from beneath clouds is difficult to retrieve. Consequently, this limits the availability of SLR data for hydrological, climatological, agricultural, and ecological research.

Cloudy surface downward longwave radiation (SDLR) has been modeled using several methods: (1) The universal Stefan–Boltzmann equation was extended by the parameterization of effective atmospheric emissivity or temperature [9]; the parameterization of effective atmospheric emissivity combines the shortwave clear-sky index to represent cloud information [9,10]. (2) Near-surface meteorological data from reanalysis datasets that are intact in space and time have been utilized to estimate all-weather SDLR. Lopes et al. [11] retrieved SDLR using a reanalysis dataset to avoid the unavailability of remote sensing retrievals and cloud information from satellite observations. (3) Parameterization of cloud-based temperature has been found to be important; however, this model also requires near-surface meteorological data from a reanalysis dataset [12] or Moderate Resolution Imaging Spectroradiometer (MODIS)-derived atmospheric profiles [13] and a satellite-derived cloud fraction. (4) The cloud water path was also used to construct retrieval models [14]. To date, studies on cloudy-sky SULR estimation are largely absent. All-weather SULR can be estimated based on the TIR radiative transfer equation which requires land surface temperature (LST), broadband emissivity, and surface downward longwave radiation (SDLR). Each component requires various models to reconstruct the values under the clouds with varying retrieval accuracy. The cloudy-sky SULR from the Global LAnd Surface Satellite (GLASS) is estimated using LST data extracted from MOD06/MYD06 and the GLASS broadband emissivity product but ignores the component of reflected cloudy-sky SDLR [15]. These algorithms are most reliable without significant cloud cover and during the daytime, since certain parameters (e.g., cloud properties) only can be retrieved from solar reflectance observations by spaceborne platforms.

Compared with optical remote sensing, passive microwaves (PMWs) have longer wavelengths, and thereby the ability to penetrate weather phenomena such as clouds, light rain, and fog, enabling all-day and all-weather observations. In areas such as deserts, PMW is able to penetrate to a certain depth so that below ground signals that are covered by vegetation or sand can be directly measured. An important milestone of space-borne PMW sensing was the Scanning Multichannel Microwave Radiometer (SMMR), launched in 1978. Since then, many sensors/satellites have been launched, including the Special Sensor Microwave/Imager (SSM/I) in 1987, Advanced Microwave Scanning Radiometer for Earth Observing System (AMSR-E) in 2002, the Special Sensor Microwave Imager/Sounder (SSMIS) in 2003, Soil Moisture and Ocean Salinity (SMOS) in 2009, Advanced Microwave Scanning Radiometer 2 (AMSR2) in 2012, Global Precipitation Measurement Microwave Imager (GMI) in 2014, and Soil Moisture Active Passive (SMAP) in 2015. Satellite PMW measurements are expected to play an important role in monitoring climate change and the hydrological cycle and have unique advantages in estimating surface parameters owing to the availability of long-term and global observation data.

Multi-channel and dual-polarized PMW measurements have been applied to retrieve geophysical parameters related to the atmosphere and land/sea surface, including land/sea surface temperature [16,17], land emissivity [18], soil moisture [19], vegetation optical depth [20], precipitation [21], cloud liquid water path [22], and column water vapor [23]. It is therefore possible to estimate all-weather SLR. In addition, PMW surface emissivity is sensitive to soil moisture and surface roughness, and thus varies widely over the land surface compared with the measurement footprint; as such, surface emissivity is inherently difficult to accurately determine and causes large uncertainties in surface temperature from PMW data [24]. However, SLR retrievals using hybrid methods implicitly avoid the determination of surface microwave emissivity, and as a result, have certain advantages in modeling and retrieval [25]. Few studies have been dedicated to estimating SLR from PMW measurements. A nonlinear regression model was constructed based on the radiative transfer simulations to estimate SDLR from SSM/I measurements [26]. Liu et al. [27] further employed a neural network model to calculate the net longwave radiation at the sea surface from SSM/I observations. These studies are aimed to retrieve SLR over oceanic regions.

For the first time, we proposed SLR retrieval models applicable to land and oceanic regions based on an AMSR2 and the European Centre for Medium-Range Weather Fore-

casts (ECMWF) Reanalysis v5 (ERA5) data using a neural network (NN) approach. SLR from ERA5 was used as ground "true" values at 25 km spatial resolution to train SLR models. They achieved good performances against the Baseline Surface Radiation Network (BSRN) and Global Tropical Moored Buoy Array (GTMBA) measurements for land and oceanic sites. Taking advantage of TIR and PMW data, the all-weather SLR data from PMW measurements can be used in combination with satellite TIR retrievals or ground observations to generate high-resolution, reliable, and spatiotemporally continuous SLR products in support of global long-term climate research.

2. Data

2.1. AMSR2 Data

The AMSR2 is a passive microwave instrument aboard the Global Change Observation Mission Water "SHIZUKU" (GCOM-W) satellite launched on 18 May 2012. AMSR2 measures multifrequency microwave radiation emitted from the Earth's surface and atmosphere from a 700-km polar orbit. The swath width of AMSR2 is 1450 km, and thereby near-global coverage can be acquired every 2 days. The frequency characteristics are shown in Table 1. The seven channels from 6.925 to 89 GHz have vertical and horizontal polarizations observed at an incidence angle of 55° relative to the Earth's surface, providing richer atmospheric and surface information, and yielding a total of 14 potential channels for SLR retrieval. Channels at 6.925 GHz and 7.3 GHz are used to mitigate radio frequency interference (RFI). In addition, AMSR2 data have improved horizontal resolution and better radiometric calibration, which improve the accuracy of retrieval products. The fields of view of 89.0 GHz (A) and 89.0 GHz (B) have an incidence angle difference of 0.5° because of the feedhorn alignment [28], and measurements in 89.0 GHz (A) with a 55.0° incident angle were used. The AMSR2 Level 3 (L3) daily brightness temperature (BT) product has a global equirectangular projection in ascending (13:30 local time) and descending (01:30 local time) orbits, and two grid sampling resolutions: 10 and 25 km. The SLR models were trained using L3 BT products with 25 km grid sampling resolution in 2019, and the trained models were validated using 2016–2018 and 2020 data.

Table 1. Channel characteristics of the Advanced Microwave Scanning Radiometer 2 (AMSR2) [28]. Each observation frequency has vertical (V) and horizontal (H) polarizations. The measuring range of each channel is 2.7−340 K. NEΔT: noise equivalent differential temperature; IFOV: instantaneous field of view.

Short Name	Frequency (GHz)	Bands	NEΔT (K)	IFOV (km^2)
T6H/T6V	6.925	C	0.34	35 × 62
T7H/T7V	7.3	C	0.43	34 × 58
T10H/T10V	10.65	X	0.70	24 × 42
T18H/T18V	18.7	K	0.70	14 × 22
T23H/T23V	23.8	K	0.60	15 × 26
T36H/T36V	36.5	Ka	0.70	7 × 12
T89H/T89V	89.0 (A)	W	1.20	3 × 5
\	89.0 (B)	W	1.20	3 × 5

2.2. ERA5 Reanalysis Data

The ERA5 climate reanalysis product is the fifth and most recent generation of atmospheric reanalysis of the global climate produced by the ECMWF, which started in the 1980s [29]; it offers significant improvements on its predecessors (e.g., ERA-15, ERA-40, and ERA-Interim). ERA5 provides hourly analysis fields on a 0.25° latitude and longitude grid for a large number of essential atmospheric, terrestrial, and oceanic climate variables from 1979 onward. The reanalysis data integrate satellite observations and ground measurements into the data assimilation system and provide complete coverage of the Earth's surface, which is in contrast to satellite-derived geophysical parameters that suffer data gaps owing to clouds and swath width. The ERA5 uses the Radiative Transfer for TOVS (RTTOV)

model version 11 [30] to model radiative transfer in optical and microwave spectra in all weather conditions, including cloudy and precipitating atmospheres [29].

The basis for the current AMSR2 SLR modeling is the accuracy and long-term stability of ERA5 SLR data at the global scale. The SDLR product of the ERA5 dataset has the best performance among the state-of-the-art reanalysis products over the global surface [31], and overall better accuracy in the three poles [5]. Tang et al. [32] found that the hourly ERA5 SDLR product had a bias of -4.9 W/m^2, RMSE of 21.9 W/m^2, and R^2 of 0.92 when validated using measurements from 46 BSRN land stations. Another recent evaluation indicated that ERA5 SDLR had an RMSE of 22.08 W/m^2 and bias of -5.25 W/m^2 based on valid observations from 23 BSRN sites between 2004 and 2019 [11]. These results demonstrate the good performance of ERA5 data in representing global longwave radiation fields.

In this study, we used "mean surface downward longwave radiation flux" and "mean surface net long-wave radiation flux" at each hour from the ERA5 product; this corresponds to approximately the 4–100 μm portion of the spectrum. SULR was calculated by the difference between two flux values. In addition, land-sea mask and surface geopotential height data from the ERA5 (25 km) and ERA5-land (10 km) static auxiliary datasets were used to discriminate land/sea conditions and to calculate the surface altitude for each pixel of AMSR2 data, respectively.

2.3. BSRN Measurements

We validated the estimated AMSR2 SLR at land sites using global data from BSRN [33]. BSRN measures SULR/SDLR by pyrgeometers with high accuracy of 5–10 W/m^2 [34,35], and at high temporal resolution (3 min before 2009, and 1 min from 2009). It has observation stations around the world, as shown in Figure 1 and Table S1 on Supplementary Material, representing different climate regions and land cover, which were used in this study. Data processing followed the approach described by Jiao and Mu [25].

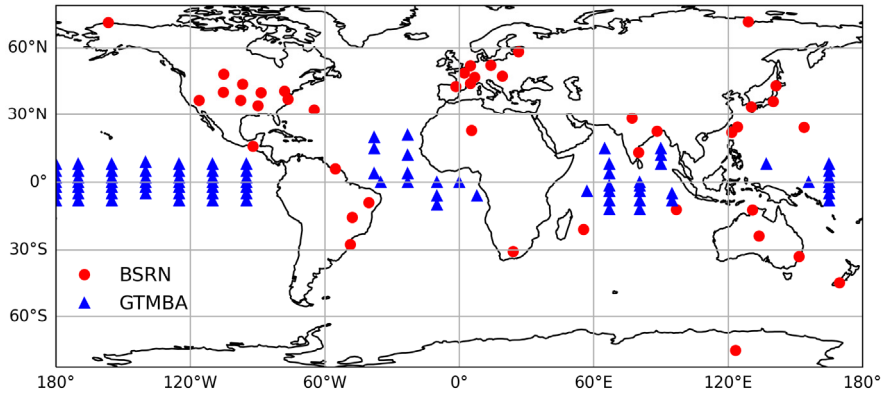

Figure 1. Spatial distribution of Baseline Surface Radiation Network (BSRN) stations (red dots) over the global land surface and Global Tropical Moored Buoy Array (GTMBA) buoy stations (blue triangles) over the ocean.

2.4. GTMBA Measurements

GTMBA provides long-term upper oceanic and atmospheric data from moored buoy platforms in real-time. It includes the Tropical Atmosphere Ocean (TAO)/Triangle Trans-Ocean Buoy Network (TRITON) array in the Pacific, Prediction and Research Moored Array in the Tropical Atlantic (PIRATA) in the Atlantic, and Research Moored Array for African-Asian-Australian Monsoon Analysis and Prediction (RAMA) in the Indian Ocean [36,37]. The spatial distribution of GTMBA sites is shown in Figure 1 with blue triangles. SDLR is measured at a height of 3.5 m above mean sea level, and the temporal resolution is either 2 min or 1 h. No SULR is observed by GTMBA; therefore, sea surface temperature (SST) was used to calculate SULR assuming blackbody emissions. SST was measured at 1 m below the sea surface, and its temporal resolution was either 10 min or 1 h.

3. Methods

Development of the proposed SLR retrieval algorithm included several steps (Figure 2). The candidate inputs into SLR models consisted of 14 BT bands of AMSR2 for ascending or descending data, as well as auxiliary data (land/sea mask and surface elevation). Invalid pixels of AMSR2 BT, which are caused by active rain or RFI, were removed. Then, the quality-checked features were collocated with SULR/SDLR from ERA5 products both spatially and temporally, generating a daily matched dataset consisting of AMSR2 BT, ERA5 SULR and SDLR, the land/sea mask, and surface elevation data. A feature selection procedure was performed to obtain optimal features for model inputs. The daily dataset with selected input parameters was divided into training, validation, and holdout datasets for model training. The optimal NN structure was first evaluated based on the above training datasets. Then, because NN-based model coefficients were randomly initialized, the NN-based SDLR and SULR models were trained 10 times to select the model with the best fitting performance. The trained models using 25-km AMSR2 data were applied to 10-km AMSR2 data. These retrieved AMSR2 SULR/SDLR data were validated using BSRN and GTMBA measurements.

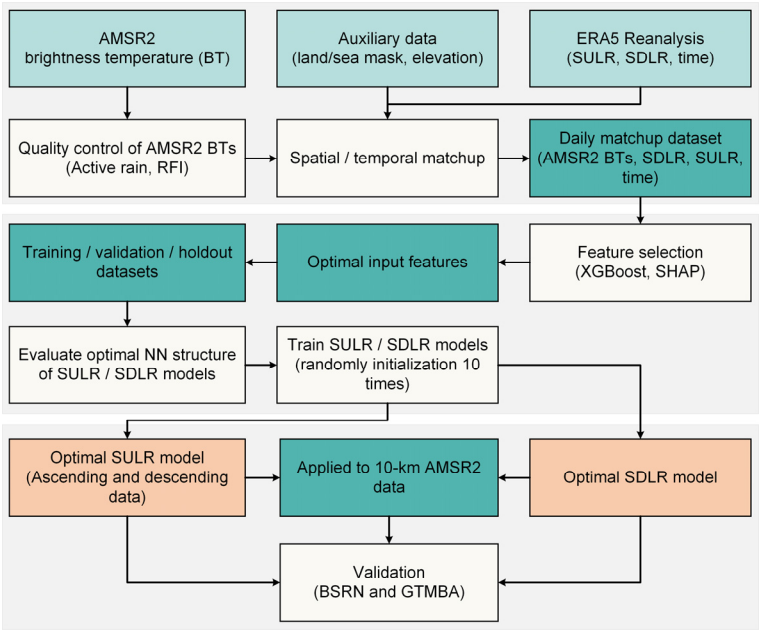

Figure 2. Workflow of constructing a retrieval model for all-weather surface longwave radiation from the Advanced Microwave Scanning Radiometer 2 (AMSR2) data. BSRN: baseline surface radiation network. ERA5: European centre for medium-range weather forecasts reanalysis v5. GTMBA: global tropical moored buoy array. NN: neural network. RFI: radio frequency interference. SDLR: surface downward longwave radiation. SHAP: Shapley additive explanation. SULR: surface upward longwave radiation.

3.1. Physical Basis for SLR Retrievals from PMW Data

Under the clear-sky condition, approximately 80% of the SDLR comes from the atmosphere within the lowest 500 m [38], which is mainly controlled by the atmospheric profiles of near-surface temperature and water vapor. The cloud covers prevent the escape of upward longwave flux and impose another thermal emitter on the SDLR. AMSR2-polarized BTs at different frequencies contain information from the atmosphere and ground surface and can reflect the core information needed to retrieve SLR.

From the perspective of the radiative transfer theory, these parameters are correlated in model retrievals based on satellite PMW measurements. For a parallel plane and non-scattering atmosphere, based on the Rayleigh–Jones law, the BT $T_{B,p}(\nu,\theta)$, in units of

Kelvins, received by the satellite microwave radiometer in the corresponding frequency v, polarization model p, and viewing angle θ, can be expressed as

$$T_{B,p}(\nu,\theta) = \varepsilon_{s,p}(\nu,\theta)T_s\Gamma(\nu,\theta) + T_a^{\uparrow}(\nu,\theta) + T_a^{\downarrow}(\nu,\theta)\big(1-\varepsilon_{s,p}(\nu,\theta)\big)\Gamma(\nu,\theta) + T_{CB}\big(1-\varepsilon_{s,p}(\nu,\theta)\big)\Gamma^2(\nu,\theta) \quad (1)$$

where $\varepsilon_{s,p}(\nu,\theta)$ is surface microwave emissivity; T_s is surface temperature; $\Gamma(\nu,\theta)$ is atmospheric transmissivity, which is related to atmospheric optical thickness; $T_a^{\uparrow}(\nu,\theta)$ and $T_a^{\downarrow}(\nu,\theta)$ are upwelling and downwelling atmospheric radiation, respectively; and T_{CB} is the cosmic microwave background equivalent of a thermal blackbody spectrum at a temperature of ~2.73 K. The PMW radiative transfer process consists of emissions from the surface, extinction and emissions through the atmosphere, and reception by spaceborne sensors within the same landscapes of the earth−atmosphere system. Radiative transfer calculations demonstrate the close correlation of PMW measurements with SLR [26]. The BTs measured by PMW sensors contain information about the downward radiation because of various microwave reflectivity at the land/sea surface. Furthermore, the downward PMW radiation is linearly correlated to the differences between vertically and horizontally polarized BTs [27], which are highly associated with SLR because of the dependence mainly on near-surface air temperature and moisture, surface temperature and emissivity, and cloud properties.

3.2. Quality Control of AMSR2 BT

To generate the training dataset, low data quality and radiometric contamination were first identified and labeled for AMSR2 ascending and descending data to guarantee the robustness of the SLR models. Two situations were excluded: (1) active rain and (2) RFI. Active rain was identified when T23V − T89V > 8 K and T89H < 270 K (see the documentation of "Algorithm Theoretical Basis Document: GCOM-W1/AMSR2 Precipitation Product"). Channels at 6.925 and 10.65 GHz are strongly affected by RFI, particularly in urban regions, which varies with time [39]. Anthropogenic RFI signals are typically narrowband; as a result, only one C-band channel at 6.925 or 7.3 GHz will be affected. RFI was identified using a generalized RFI detection approach [40].

3.3. Match-Up of AMSR2 and ERA5 Data

AMSR2 and ERA5 data have the same spatial resolution (25 km that approximates 0.25°), and therefore no spatial matchup was performed. The satellite overpass time of AMSR2 L3 observation data is either the updated time of a pixel that overwrites the previous pixel at the same location or the average time of multiple observations at the same location (see the documentation of "AMSR2 Higher Level Product Format Specification" in https://gportal.jaxa.jp, accessed on 13 October 2022). Meanwhile, the ERA5 products are hourly average data. According to the time of each pixel recorded by the L3 product, the linear weighted average of ERA5 SLR based on time differences was calculated to match each pixel of AMSR2 data in order to maintain temporal consistency. Finally, daily AMSR2 BT data for both ascending and descending orbits were matched to SLR data from ERA5.

3.4. Feature Selection from Input Parameter Candidates

PMW remote sensing has the ability to provide all-weather observations of the earth−atmosphere system but is also subject to different atmospheric influences for different frequencies and polarization modes. We took full advantage of all available information in the AMSR2 radiometric channels and selected the most sensitive bands for SULR and SDLR retrievals. Such a procedure reduces computation time and redundant information among AMSR2 frequencies without having a significant impact on estimation accuracy.

The NN-based model could not be directly used to evaluate the input feature importance based on the synchronous AMSR2 and ERA5 data. Considering the popularity and nonlinear fitting capacity of tree-based machine learning models, the SLR models were first

trained using the XGBoost library and were then input into the Shapley additive explanation (SHAP) approach to evaluate the feature importance of candidate input features. The value of feature importance approximates the degree of significance of input features in the training samples. Daily matched datasets were randomly extracted in a small percentage (i.e., 20%) to generate a subset dataset for XGBoost model training.

As an optimized distributed gradient boosting library, XGBoost provides a parallel boosting trees algorithm under the gradient boosting framework to solve machine learning tasks, such as classification and regression problems [41]. It has high prediction accuracy and the capability to capture interactions between features without explicitly defining such relationships. The SHAP method was used to explain the output of the tree-based model using Shapley values. The SHAP technology is based on a game-theoretic approach that is often used for optimal credit allocation and has been used to explain the prediction results of an ensemble tree model to increase the reliability of model prediction [42]. The SHAP value evaluates how each feature contributes to the model prediction. It is calculated by hiding each feature from the model one at a time and calculating the mean magnitude change in the output of the machine learning model. The joint contribution of interactive features was estimated based on the Shapley interaction index, enabling the consistency and accuracy of feature importance assessment.

3.5. NN-Based Model Training

A feed-forward multilayer perceptron NN model was used to build the SLR retrieval models. This model has a strong nonlinear fitting ability and high adaptability to achieve high prediction accuracy in classification and regression problems. It can simplify complex physical models and processes by learning the statistical relationship between input and output parameters from the training dataset. Therefore, NN models are widely used in the geoscience and remote sensing communities [43,44] and are valuable tools to explore the estimation of SLR using multifrequency PMW radiation from satellite observations. In this study, the sample dataset for the NN-based model was derived using the aforementioned procedures. The daily global BT data had 720 rows and 1440 columns, resulting in a total of approximately 1 million samples per day, which were divided into training (70%), validation (20%), and holdout (10%) datasets. The training dataset was used to train corresponding retrieval models; the validation dataset was used to check the training process to avoid over- or under-fitting; and the independent holdout dataset was used as the final benchmark to evaluate the model fitting performance. The data from each day were input to train the SULR/SDLR models, and the models were continuously trained 365 times (i.e., 365 days in 2019).

The NN-based models had an input layer, one to two hidden layers using a rectified linear unit activation function, and an output layer with one neuron using a linear activation function. The Adam optimization algorithm was used to implement fast and reliable model training. To avoid network overfitting and to enhance the generalization capability of NN models, regularization of input features and an early stopping technique was used. The early stopping method can reduce training epochs to minimize overfitting and accelerate model training. The model parameters were randomly initialized, resulting in slightly different final NN parameters and SLR retrieval accuracy. Therefore, each training was repeated 10 times, and we chose the optimal trained model according to the fitting performance using the holdout dataset. We constructed daytime and nighttime models using ascending and descending data, respectively, in order to improve model fitting performances.

The NN structure or topology (i.e., the number of hidden layers and neurons in each hidden layer) is the hyperparameter that is required to be determined before the model was trained. Different NN structures were tested based on selected input features (see Section 4.1) to identify the optimal network structure (i.e., with the lowest RMSE and bias and highest R^2, estimated using the holdout dataset; Figure 3). The single hidden layer had a relatively weaker performance. The structure of 16 × 8 had fewer neurons,

simpler topology, and a relatively better performance, with a bias of -1.43 W/m^2, RMSE of 18.59 W/m^2, and R^2 of 0.97. SDLR is a more complex geophysical parameter than SULR when estimated using BT at the top-of-atmosphere (TOA). Therefore, more complex network topologies were used (Figure 4). When the size of the NN structure was larger than 32 × 8, all structures showed a similar performance; finally, the 32 × 16 structure was chosen.

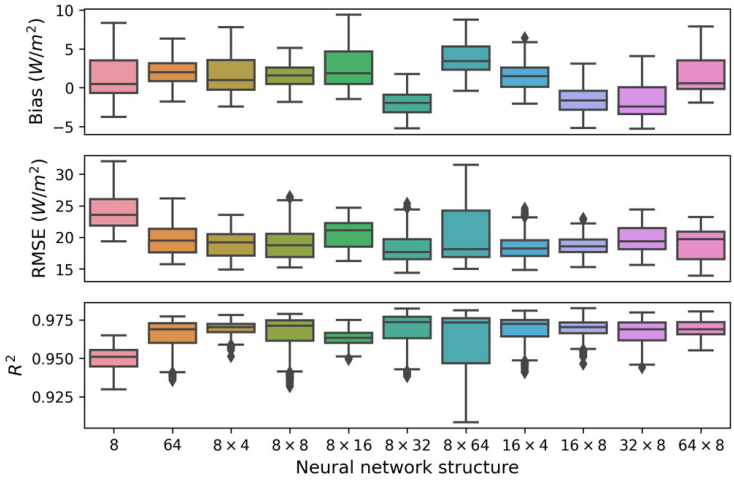

Figure 3. Performances of different neural network (NN) structures for surface upward longwave radiation (SULR) estimation. The metrics are bias, root mean square error (RMSE), and R^2 from top to bottom. Each NN structure was trained 10 times. The "8" indicates a single hidden layer with eight neurons, and "8 × 4" indicates two hidden layers in which the first layer has eight neurons, and the second layer has four neurons. The 16 × 8 structure showed the best performance.

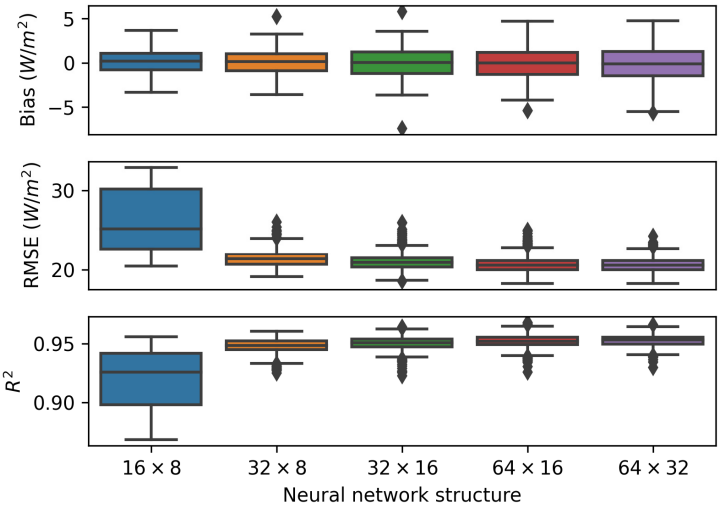

Figure 4. Performances of different neural network (NN) structures for surface downward longwave radiation (SDLR) estimation. The metrics are bias, root mean square error (RMSE), and R^2 from top to bottom. Each NN structure was trained 10 times. The "16 × 8" indicates two hidden layers in which the first layer has 16 neurons, and the second layer has 8 neurons. The 32 × 16 structure showed the best performance.

3.6. Validation and Evaluation Metrics

The spatial and temporal matchup is essential to valid accuracy assessment. The spatial representativeness of ground sites is crucial for the coarse spatial resolution (i.e., 10 and 25 km) of the AMSR2 L3 product [45]. In general, the sea surface is considered thermally homogenous, and locations of BSRN sites are always chosen in relatively homogeneous

surfaces [33]. As a simple and effective method, the pixel containing the ground station is selected as the retrieval value [5,6,14,32,46], representing a reasonable approximation, although the unresolved uncertainties due to the spatial representativeness issue should be realized [19,31] because the thorough investigation of spatial representativeness of BSRN and GTMBA in terms of SLR observations has not yet been reported.

In this work, AMSR2 overpass time data were used to match the time of ground-based SLR measurements from BSRN and GTMBA. Pixels of AMSR2 data that contained ground sites were extracted to obtain satellite-derived SLR values. The quality check described in Section 3.2 was performed to acquire high-quality retrievals. BSRN and GTMBA measurements have various temporal resolutions, with the longest interval of 1 h (see Sections 2.3 and 2.4). The 1-h average of ground measurements was used as the ground truth value to match the AMSR2-derived SLR [47]. Three statistical metrics were used to evaluate the retrieval accuracy of the proposed SLR models: the mean bias error (bias), RMSE, and the coefficient of determination (R^2), which are defined as follows:

$$\text{Bias} = \frac{1}{N}\sum_{i=1}^{N}(X_{i,\ retrieval} - X_{i,\ \ true}) \tag{2}$$

$$\text{RMSE} = \sqrt{\frac{1}{N}\sum_{i=1}^{N}(X_{i,retrieval} - X_{i,true})^2} \tag{3}$$

$$R^2 = \frac{\left[\sum_{i=1}^{N}\left(X_{i,true} - \overline{X_{true}}\right)\left(X_{i,\ retrieval} - \overline{X_{retrieval}}\right)\right]^2}{\sum_{i=1}^{N}\left(X_{i,true} - \overline{X_{true}}\right)^2 \cdot \sum_{i=1}^{N}\left(X_{i,\ retrieval} - \overline{X_{retrieval}}\right)^2} \tag{4}$$

where N is the total count of validation samples; $X_{i,\ retrieval}$ is the retrieved SULR/SDLR value for the ith sample; $X_{i,\ true}$ is the true SULR/SDLR value for the ith sample, which is the ground measurement; $\overline{X_{true}}$ is the mean of all $X_{i,true}$; and $X_{retrieval}$ is the mean of all $X_{i,\ retrieval}$.

4. Results

4.1. Selected Features for Model Inputs

The SHAP value was used to quantify input feature contributions to model output (Figure 5). The values of Mean(|SHAP|) (δ) declined smoothly to a stable value. Band T89V always had the highest δ, and features with $\delta > 5$ were selected as the model inputs considering the trend variations in Figure 5 and retaining as few features as possible, as summarized in Table 2. The seven most important features for the SULR models were the same for both AMSR2 ascending and descending data (Table 2), with the exception that bands T89H and T36V were selected for AMSR2 ascending and descending data, respectively. Both SDLR models for AMSR2 ascending and descending data shared the same input features. They represented the most significant contributions to SULR/SDLR variation in ERA5 data. T06 V/H was significantly impacted by RFI effects for various locations and times, resulting in some anomalous retrievals.

SULR is associated with LST and surface emissivity, while SDLR mostly depends on near-surface water vapor and air temperature. Water vapor is the most important factor affecting the TOA BT variation of AMSR2 under clear sky conditions. Meanwhile, cloud liquid water has the strongest impact on the TOA BT under cloudy or overcast conditions, and the magnitude becomes greater with a higher PMW frequency. In general, high frequencies are more sensitive to the atmosphere, including clouds, while low frequencies are more sensitive to the Earth's surface. Vertically polarized 89 GHz was used to decrease the average influence of the atmosphere. The high-frequency channels (e.g., 36.5 and 89 GHz) of AMSR2 are significantly affected by water vapor, while atmospheric effects can be ignored for AMSR2 channels at 6.925, 7.3, and 10.65 GHz. Vertically polarized

BT differences at 36.5 and 23.8 GHz can attenuate the influence of atmospheric water vapor [48].

In operational retrieval practices, BTs at 18.7, 23.8, 36.5, and 89.0 GHz have been used for LST and land emissivity [49–51], and show high reliability for the accurate estimation of the cloud liquid water path [51,52]. The atmospheric transmittances of T18, T23, and T36 have the strongest correlation with column water vapor contents [23,51]. The NN-based models integrate these PMW channels using complex nonlinear structures to find the best coefficients to estimate SULR/SDLR.

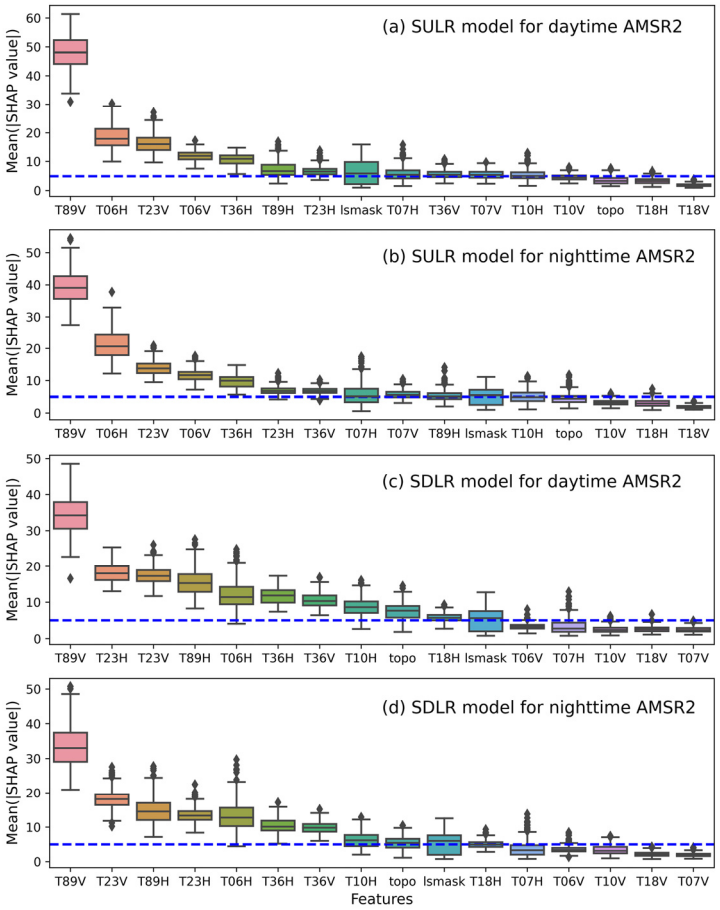

Figure 5. Histograms of the feature importance of surface upward/downward longwave radiation (SULR/SDLR) models based on the Shapley additive explanation (SHAP) method using daily calculation results from 2019. The blue dashed line indicates the Mean(|SHAP|) value of 5.

Table 2. Optimal features for neural network (NN)-based surface upward/downward longwave radiation (SULR/SDLR) model inputs for the ascending (ASC) and descending (DES) data of the Advanced Microwave Scanning Radiometer 2 (AMSR2).

No.	SULR ASC	SULR DES	SDLR ASC/DES
1	T89V	T89V	T89V
2	T06H	T06H	T23H
3	T23V	T23V	T23V
4	T06V	T06V	T89H
5	T36H	T36H	T06H
6	T89H	T23H	T36H
7	T23H	T36V	T36V
8	\	\	T10H
9	\	\	Elevation

4.2. AMSR2 SLR Data Compared with ERA5 Product

ERA5 reanalysis data were used as the reference in SLR model construction. The comparison between the estimated SLR derived from AMSR2 and ERA5 data demonstrated the fitting ability of the proposed SLR models. AMSR2 and ERA5 SULR mapping showed high comparability in the spatial domain (Figure 6) on the first day of the 2020 validation dataset. AMSR2 SULR could well represent global longwave radiation variability. In the daytime ascending data, some terrestrial regions (e.g., Australia and Africa) had the highest SULR values, while oceanic SULR values were moderate. In contrast, during the nighttime for descending data, ocean regions had the highest SULR within low–middle latitudes. The differences in SULR between AMSR2 and ERA5 were low within most oceanic areas and some terrestrial regions. For example, AMSR2 SULR was overestimated in Greenland, but underestimated in Australia compared with the ERA5 SULR product. Errors in cloud properties (e.g., total cloud fraction, cloud liquid, and ice water path) in reanalysis products can cause significant biases in simulated SLR [53,54]. Moreover, the RFI effect can also contribute to this discrepancy because T06 V/H channels, which were used in the retrieval procedure, are strongly influenced by RFI effects [55].

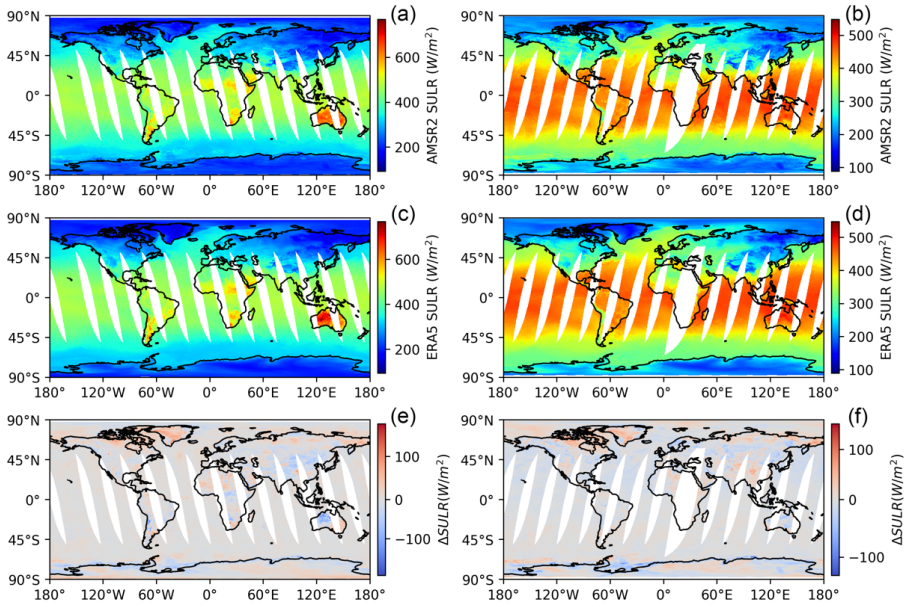

Figure 6. Comparison of the global Advanced Microwave Scanning Radiometer 2 (AMSR2) and European Centre for Medium-Range Weather Forecasts (ECMWF) Reanalysis v5 (ERA5) surface upward longwave radiation (SULR) data from 1 January 2020. (**a**) AMSR2 SULR derived from ascending data; (**b**) AMSR2 SULR derived from descending data; (**c**) ERA5 SULR matched with ascending data; (**d**) ERA5 SULR matched with descending data; (**e**) difference between AMSR2 and ERA5 SULR for ascending data; and (**f**) difference between AMSR2 and ERA5 SULR for descending data.

Although global SDLR had a complex spatial distribution, principally due to cloud effects [13,56], the spatial patterns of AMSR2 and ERA5 SDLR showed good consistency (Figure 7). The day/night differences in SDLR over land and ocean were small compared with those of SULR (Figure 6). Cloud cover at low to medium altitudes significantly enhances SDLR [10,13], as shown by the cyclone system in the Atlantic region (Figure 7b,d). ERA5 SDLR had smoother transitions than AMSR2 SDLR, as shown in Eurasia, indicating the impact of surface radiative characteristics on SDLR retrievals. In general, the NN-based SLR models could reproduce the global spatial distribution of SULR/SDLR from AMSR2 data using ERA5 as a baseline. Validation based on ground measurements on both land and ocean was performed to offer quantitative accuracy metrics.

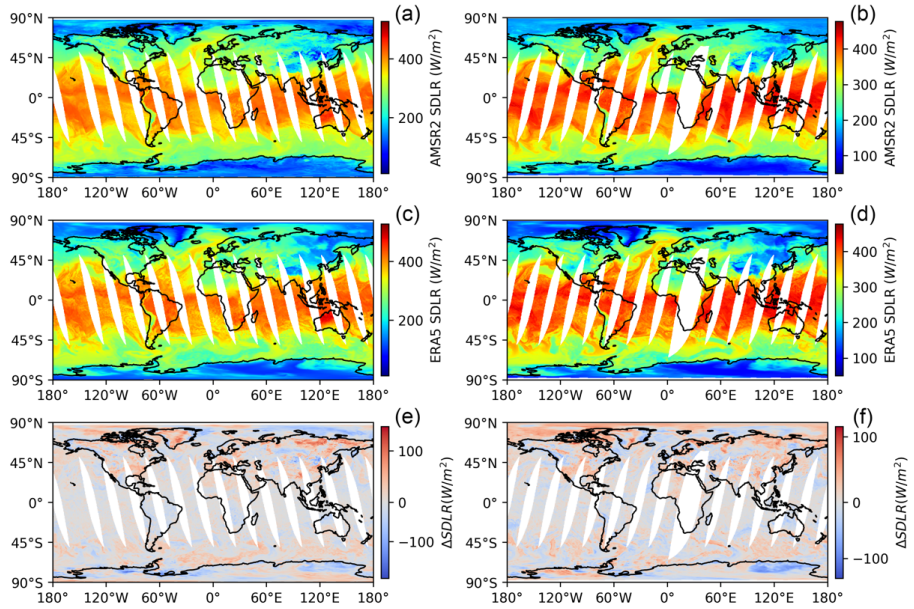

Figure 7. Comparison of the global Advanced Microwave Scanning Radiometer 2 (AMSR2) and European Centre for Medium-Range Weather Forecasts (ECMWF) Reanalysis v5 (ERA5) surface downward longwave radiation (SDLR) data from 1 January 2020. (**a**) AMSR2 SDLR derived from ascending data; (**b**) AMSR2 SDLR derived from descending data; (**c**) ERA5 SDLR matched with ascending data; (**d**) ERA5 SDLR matched with descending data; (**e**) difference between AMSR2 and ERA5 SDLR for ascending data; and (**f**) difference between AMSR2 and ERA5 SDLR for descending data.

4.3. Validation over BSRN Land and GTMBA Oceanic Sites

Based on BSRN measurements, SLR derived from AMSR2 data had promising performances (Figure 8). Slight underestimations of 1.32 W/m^2 existed for SULR, and the bias was −2.26 W/m^2 for AMSR2 SDLR estimation (Figure 8a,c). The RMSE and R^2 of AMSR2 SULR were 35.37 W/m^2 and 0.89, respectively. At higher SULR values, those from AMSR2 diverged, indicating the degradation of model performance. At the same time, AMSR2 SULR of <200 W/m^2 in high-altitude and polar regions showed a conspicuous overestimation that can also be found in CERES-derived fluxes [46]. The SDLR model for AMSR2 had an RMSE of 32.94 W/m^2 and R^2 of 0.82, which demonstrate a good agreement with land site observations (Figure 8c).

The thermal homogeneity of the ocean is always higher than that of the land. Oceanic thermal radiation can be treated as quasi-blackbody emissions that can well satisfy the Lambertian surface assumption and facilitate sufficient spatial representativeness of site measurements [45]. The validation results were significantly better than those on land (Figure 8). The biases showed a few underestimations, and the RMSEs of AMSR2 SULR were 6.50 W/m^2 (Figure 8b), which was even better than the measurement accuracy of pyrgeometers (5−10 W/m^2) [34,35]. SULR with a high retrieval accuracy, as an alternative to SST, can be used in monitoring climate phenomena, such as the El Niño–Southern Oscillation and La Niña [4]. On the other hand, underestimations of SDLR derived from AMSR2 data based on GTMBA data were −4.04 W/m^2 (Figure 8d). AMSR2 BT had a stronger correlation with SULR, which emits PMW radiation directly into space-based radiometers through the atmosphere. Meanwhile, the RMSE showed a better accuracy according to the retrieval models using MODIS data [25]. In summary, the accuracy of the ASMR2 SLR over the ocean was significantly better than that on land that has more complex surface and thermal conditions.

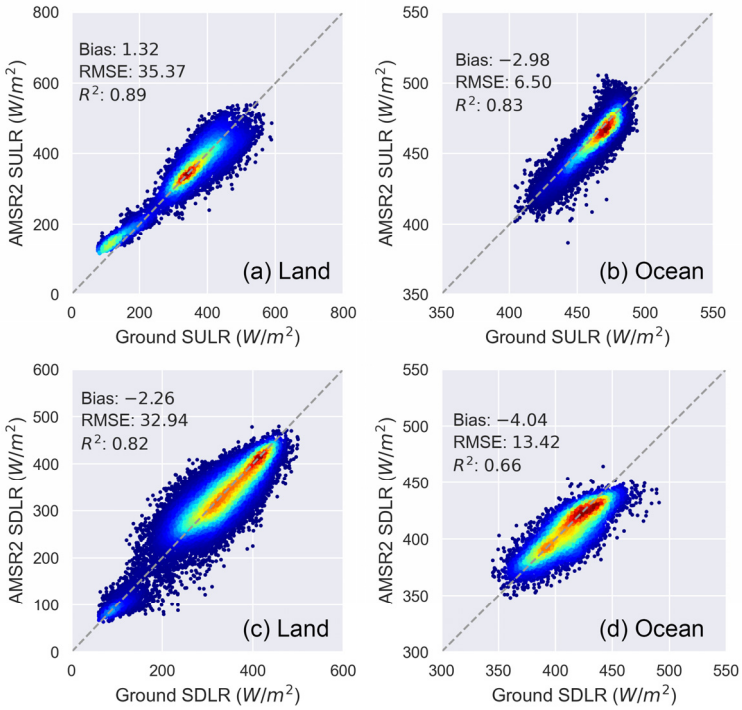

Figure 8. Validations for (**a**) surface upward longwave radiation (SULR) and (**c**) surface downward longwave radiation (SDLR) derived from the Advanced Microwave Scanning Radiometer 2 (AMSR2) using Baseline Surface Radiation Network (BSRN) measurements and for (**b**) SULR and (**d**) SDLR derived from the AMSR2 using the Global Tropical Moored Buoy Array (GTMBA) measurements. The color indicates the density of sampling points, with higher density in red and lower density in blue.

5. Discussion

5.1. Impact of Surface Types

The BSRN observation sites were divided into different surface types, including island, continental, desert, coastal (~25 km from the coastal line), and polar sites [46]. The validation results shown in Table 3 were used to analyze the retrieval accuracy on major surface types. For SDLR validation, polar sites showed a high R^2 of 0.91 and a good RMSE of 22.88 W/m^2. In addition, island sites also had a lower RMSE of 20.66 W/m^2, where the land occupies a small percentage, and the emitted radiation was from the dominant ocean surface. High surface heterogeneity at coastal sites made the spatial representativeness of ground measurements relative to the AMSR2 footprint worse, causing a larger RMSE. The desert sites had the largest bias (−12.77 W/m^2) and a higher RMSE of 33.48 W/m^2. There was a significant overestimation (17.54 W/m^2) for the SULR estimation at polar sites, and the largest RMSE of 43.36 W/m^2 was at coastal sites. The surface type has a significant impact on the estimated AMSR2 SLR [46], while the spatial representativeness of ground-based sites is another important influence factor that compromises the robustness of the validation of low spatial resolution data [45], which has largely been ignored.

Table 3. Comparison between surface-measured and AMSR2-derived surface upward and downward longwave radiation (SULR/SDLR) components for the coastal, continental, desert, island, and polar sites on land. The units of both bias and root mean square error (RMSE) are W/m^2. Note that no SULR measurements were available at the island and desert sites.

Type	Bias	RMSE	R^2
		SDLR	
Island	−0.62	20.66	0.50
Coastal	−5.33	35.68	0.67
Polar	−4.47	22.88	0.91
Continent	0.30	34.70	0.61
Desert	−12.77	33.48	0.66
		SULR	
Coastal	−1.02	43.36	0.53
Polar	17.54	27.15	0.94
Continent	−4.26	36.22	0.60

5.2. Analysis of Day/Night Effects

Based on BSRN measurements, there was a significant overestimation (13.96 W/m^2) of land SULR in the daytime and an underestimation (−11.09 W/m^2) in the nighttime for AMSR2 data (Table 4). Consequently, the overall validation biases including daytime and nighttime samples had smaller values. The SULR at the daytime and nighttime had similar performances, with RMSEs of 35.02 and 35.70 W/m^2. For the oceanic SULR samples, the day/night differences were considerably lower, although daytime validation had a better performance than that in the nighttime (i.e., less RMSE and bias). The SDLR on the land showed significant negative biases of −7.85 W/m^2 in the nighttime and overestimated by 3.24 W/m^2 in the daytime. SDLR validation based on oceanic sites revealed underestimations, and bias magnitudes (−4.91 W/m^2) in the daytime were larger than those in the nighttime. The diurnal cycle changes the temperature structure of the atmospheric boundary layer, resulting in significant discrepancies in the atmospheric thermal radiative environment. The variability of surface-atmosphere temperatures impacts the AMSR2 longwave radiation calculations.

Table 4. The validation results of the surface longwave radiation components at land and ocean sites. The units of both bias and root mean square error (RMSE) are W/m^2. SDLR: surface downward longwave radiation. SULR: surface upward longwave radiation.

Type	Bias	RMSE	R^2	Bias	RMSE	R^2
	SDLR on the land			SULR on the land		
Day	3.24	33.40	0.82	13.96	35.02	0.91
Night	−7.85	32.47	0.83	−11.09	35.70	0.92
	SDLR on the ocean			SULR on the ocean		
Day	−4.91	13.62	0.66	−0.02	4.93	0.87
Night	−3.17	13.22	0.66	−5.90	7.74	0.86

5.3. Validation of ERA5 SLR Data

The validation results for ERA5 SLR data using BSRN land and GTMBA oceanic sites are shown in Figure 9. They had similar performances as shown in Figure 8. The AMSR2-derived SDLR over the land and ocean had lower RMSEs (32.94 W/m^2 and 13.42 W/m^2, respectively) compared with those of ERA5 SDLR. Meanwhile, ERA5 SULR data had better agreement with GTMBA measurements than AMSR2 SULR data (Figure 9a,b) by about 2 W/m^2 in terms of RMSE. The underestimation of AMSR2 SULR, less than 200 W/m^2, was more significant than the ERA5 SULR on the land; in contrast, the AMSR2 model overestimated SULR in the ocean (Figure 8a), with higher values that were not observed for ERA5 SULR. The AMSR2-based SDLR has the advantage of modeling atmospheric thermal flux in all weather conditions.

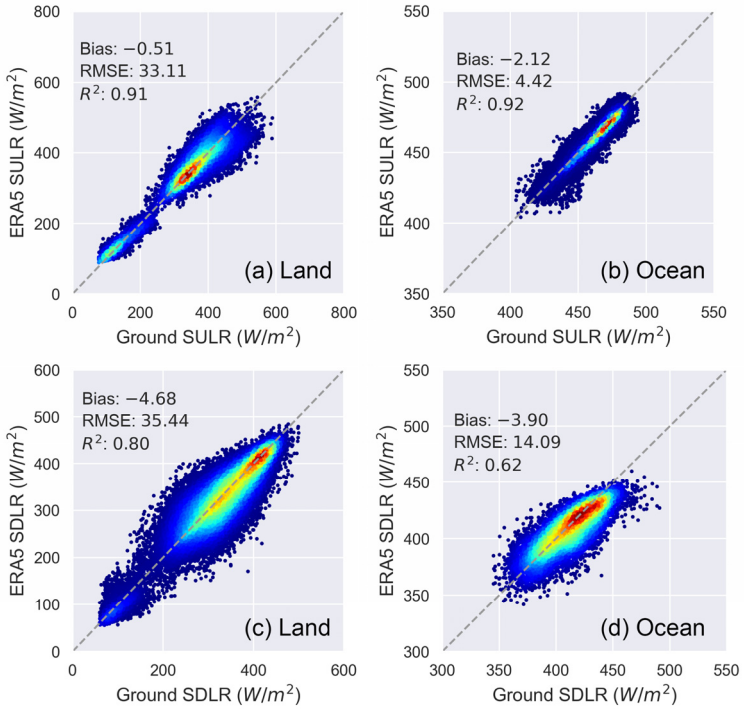

Figure 9. Validation of the European Centre for Medium-Range Weather Forecasts (ECMWF) Reanalysis v5 (ERA5) surface longwave radiation using site measurements. (**a**) ERA5 surface upward longwave radiation (SULR) based on Baseline Surface Radiation Network (BSRN) data; (**b**) ERA5 SULR based on Global Tropical Moored Buoy Array (GTMBA) data; (**c**) ERA5 surface downward longwave radiation (SDLR) based on BSRN data; and (**d**) ERA5 SDLR based on GTMBA data. The color indicates the density of sampling points, with higher density in red and lower density in blue.

5.4. Model Application on 10-km AMSR2 Data

The proposed SLR models, which were trained based on 25-km AMSR2 and ERA5 data, were applied to AMSR2 data with a grid sampling resolution of 10 km. The 10-km auxiliary data (i.e., surface elevation and land/sea mask) were obtained from the ERA5-land dataset [57]. Using AMSR2 ascending data for the same day as that shown in Figure 6 as an example, the 10- and 25-km SULR data show high consistency (Figure 10a,b). High-latitude areas had the lowest SULR values (<300 W/m^2). AMSR2 SDLR at 10 and 25 km spatial resolutions were also identical (Figure 10c,d). Regions lower than 30°N had a high SDLR for both inland and ocean areas. In Asia, the 10 km SLR data had a higher spatial variability compared with the 25 km data.

The overall validation results (Figure 11) were similar to those in Figure 8, indicating the feasibility of applying the proposed models to AMSR2 10-km data. For example, the SULR model performance at inland sites had a bias of 1.36 W/m^2, RMSE of 38.09 W/m^2, and R^2 of 0.86 for the 10 km data, and a bias of 1.32 W/m^2, RMSE of 35.37 W/m^2, and R^2 of 0.89 for the 25 km data. The validation results for the 25 km data had a generally higher accuracy, especially in terms of the RMSE. AMSR2 adapts a conical scan mechanism to acquire PMW data. The footprints (i.e., observable region) of different channels are significantly different for the same pixel. Therefore, the Backus–Gilbert method was used to obtain equivalent footprints for all channels through the synthesis of virtual observations [28]. The gridding process introduced alignment and radiometric errors in the 10-km AMSR2 product, which likely reduced the model performance. In summary, training SLR models with 25 km data and then applying them to 10-km AMSR2 data offers an alternative approach to obtaining SLR data from AMSR2 with higher spatial resolution.

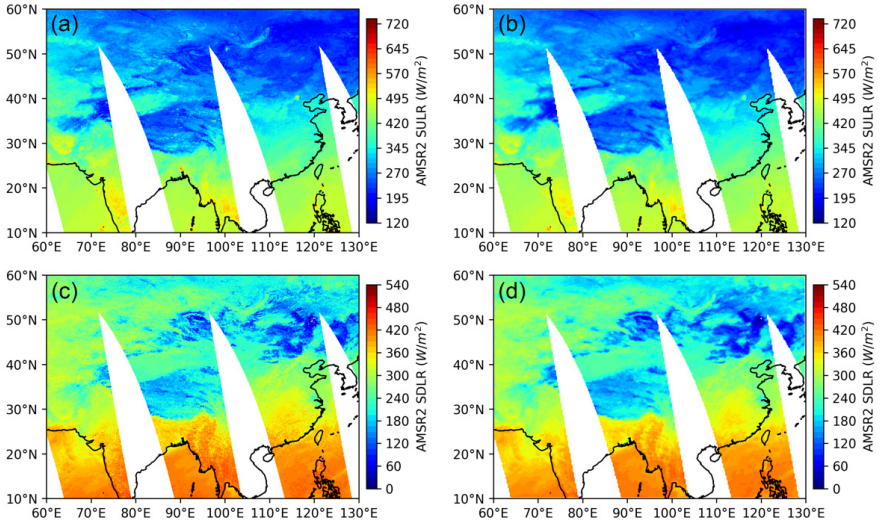

Figure 10. Comparison between the 10- and 25-km surface longwave radiation of the Advanced Microwave Scanning Radiometer 2 (AMSR2) ascending data in Asia on 1 January 2020. (**a**) AMSR2 10-km surface upward longwave radiation (SULR); (**b**) AMSR2 25-km SULR; (**c**) AMSR2 10-km surface downward longwave radiation (SDLR); and (**d**) AMSR2 25-km SDLR.

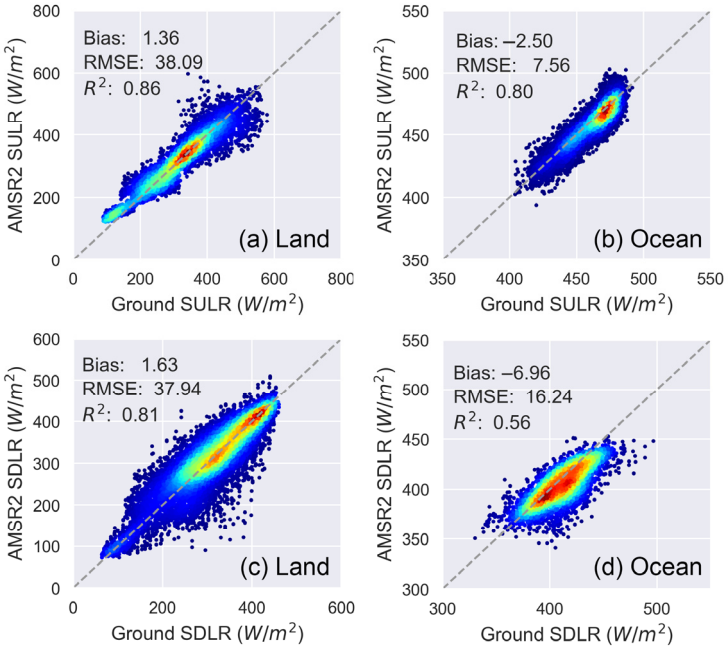

Figure 11. Validation of the 10-km Advanced Microwave Scanning Radiometer 2 (AMSR2) surface longwave radiation using site measurements. (**a**) AMSR2 surface upward longwave radiation (SULR) based on Baseline Surface Radiation Network (BSRN) data; (**b**) AMSR2 SULR based on Global Tropical Moored Buoy Array (GTMBA) data; (**c**) AMSR2 surface downward longwave radiation (SDLR) based on BSRN data; and (**d**) AMSR2 SDLR based on GTMBA data. The color indicates the density of sampling points, with higher density in red and lower density in blue.

5.5. Advantages, Limitations, and Future Works

This is the first work to demonstrate the feasibility of estimating SLR from PMW observations on both the land and ocean and provides an alternative to TIR-based SLR retrieval. Further development and maintenance of PMW-based SLR products are necessary to help us improve our insight into complex geographic areas where reanalysis datasets reach their limits in characterizing the spatial variability of geophysical parameters [58]. A

significant advantage of estimating SLR from spaceborne PMW TBs is the multi-channel PMW observations over decades, e.g., from the earliest SMMR to the current AMSR2 and FengYun-3 Microwave Radiation Imager (MWRI) series. If the inter-calibration of different PMW sensors is well performed [59], the proposed SLR model can be applied not only to 10-km AMSR2 data but also to other sensors, such as the WindSat and FY-3 MWRI series. Therefore, it is possible to generate long-term PMW-derived SLR data using a long time series and consistent PMW observations available from 1978 onwards, which have a unique value in evaluating the role of SLR in global climate change. In addition, with the development of sensor technologies, the PMW sensor can measure the earth−atmosphere system with a higher spatial resolution than current spatial resolutions of 10 and 25 km; when a PMW sensor is installed on a geostationary satellite platform, it can achieve a very high temporal resolution. These advantages relative to ERA5 data can happen in the future, and this work provides the feasibility and basis to achieve SLR retrieval from higher spatiotemporal PMW measurements.

It is essential for PMW remote sensing data to distinguish atmospheric conditions (clear sky, cloudy, rain, or mixed) over land and ocean, and different land covers. However, unlike optical sensors (e.g., MODIS), such products are not available for AMSR2. Therefore, cloud effects on the retrieval model cannot be analyzed. Land covers such as desert, snow, glacier, or sea ice, also have important influences on SLR models; their impacts should be analyzed using stable synchronous data products for quantifying uncertainties and improving SLR algorithms. Furthermore, radiative transfer in a dense vegetation canopy and precipitation was not explicitly considered in our SLR modeling. Soil moisture, the microphysical and optical properties of clouds (e.g., cloud liquid/ice water path), and the wind speed on the sea also impact PMW radiative transfer and must be confirmed in the construction of SLR retrieval models. Thorough analyses of influencing factors should be carried out for model improvement.

The combination of TIR and PMW data is a promising way to generate global long-term seamless SLR products with the same spatial resolution as satellite TIR data [60]. However, the penetrability of PMW measurements into the ground surface makes them incompatible with SLR derived from TIR remote sensing data. The transformation of PMW-derived to TIR-derived geophysical parameters (e.g., LST and SULR) remains a challenge but is the physical basis for data fusion between TIR and PMW [24]. The further development of models for estimating SLR from PMW remote sensing techniques will increasingly depend on an understanding of microwave emission theories, rather than statistical regression models.

As data-driven models, the potential functional relationships of the proposed models were learned from a training dataset. The accuracy of ERA5 SLR products is the primary factor for retrieval performance. Bias correction of ERA5 SLR products can generate better agreement with ground measurements [61], and bias-adjusted ERA5 data have the potential to improve retrieval models based on AMSR2 data. Insufficient training samples for certain conditions reduced the capability of the SLR models to accurately reproduce the spatiotemporal dynamics of global SLR. An alternative would be to generate a simulation dataset using PMW radiative transfer models (e.g., the RTTOV model) [26,27]. The inherent physical processes are coupled with data-driven models, strengthening their generalization ability under diverse atmospheric and surface conditions. Furthermore, the theoretical calculation of AMSR2 BT and SLR can perform simulation analyses on atmospheric and surface conditions, and the sensitivity of input features [52].

6. Conclusions

Satellite PMW observations have been used for various geophysical retrievals; however, surface radiation budget parameters that rely on microwave techniques have not been studied in depth. In this study, we identified the statistical relationship between AMSR2 polarized BT and SLR for both clear sky and cloudy conditions based on a multilayer NN approach. The algorithm retrieves SULR/SDLR over ocean and land areas in

a unified model, and separate algorithms are applied for ascending and descending data. The AMSR2 SLR retrieval models have a high correlation and comparable performance with respect to the ERA5 SLR products used as a reference in model training, indicating the ability of the proposed models to generate global SLR data. The SLR models were optimized using 25-km AMSR2 BT, ERA5 SLR data, and ancillary data of surface elevation. The performances of the NN-based models were validated using independent datasets of BSRN and GTMBA measurements. Generally, SULR retrievals over the ocean had a higher accuracy than those over land on account of thermal homogeneity and quasi-blackbody emissions from the ocean surface. Moreover, the AMSR2 SLR data at 10 and 25 km spatial resolutions were in good agreement with ground measurements, confirming the feasibility of the proposed SLR models for AMSR2 observations at different spatial scales. Our method demonstrates high reliability in retrieving global SLR under all weather conditions. This new algorithm is expected to promote the development of satellite-based PMW remote sensing data to generate global long-term and continuous SLR products for climate studies.

Supplementary Materials: The following supporting information can be downloaded at: https://www.mdpi.com/article/10.3390/rs14235960/s1, Table S1: Description of Baseline Surface Radiation Network (BSRN) stations used to evaluate surface longwave radiation models.

Funding: This research was funded by the National Key Research and Development Program of China, grant numbers 2020YFA0608702 and 2019YFC1509202; the National Natural Science Foundation of China, grant number 41701409; and the Basic Science Research Plan of the Institute of Geology, China Earthquake Administration, grant number IGCEA2002.

Data Availability Statement: The AMSR2 product was provided by the Japan Aerospace Exploration Agency G-Portal (https://gportal.jaxa.jp/gpr/index, accessed on 13 October 2022). The ERA5 climate reanalysis product was provided by the ECMWF (https://www.ecmwf.int/en/forecasts/datasets/reanalysis-datasets/era5, accessed on 13 October 2022). The ground-based measurements of longwave radiation were provided by the Global Monitoring Division of the National Oceanic and Atmospheric Administration (NOAA) (http://www.esrl.noaa.gov/gmd/grad/surfrad, accessed on 13 October 2022). The buoy measurements were provided by the Pacific Marine Environmental Laboratory of NOAA (https://www.pmel.noaa.gov/gtmba/mission, accessed on 13 October 2022).

Conflicts of Interest: The author declares no conflict of interest.

References

1. Liang, S.; Wang, D.; He, T.; Yu, Y. Remote sensing of earth's energy budget: Synthesis and review. *Int. J. Digit. Earth* **2019**, *12*, 737–780. [CrossRef]
2. Wild, M. The global energy balance as represented in CMIP6 climate models. *Clim. Dyn.* **2020**, *55*, 553–577. [CrossRef]
3. Wild, M. Decadal changes in radiative fluxes at land and ocean surfaces and their relevance for global warming. *WIREs Clim. Chang.* **2015**, *7*, 91–107. [CrossRef]
4. Rädel, G.; Mauritsen, T.; Stevens, B.; Dommenget, D.; Matei, D.; Bellomo, K.; Clement, A. Amplification of El Niño by cloud longwave coupling to atmospheric circulation. *Nat. Geosci.* **2016**, *9*, 106–110. [CrossRef]
5. Wang, G.; Wang, T.; Xue, H. Validation and comparison of surface shortwave and longwave radiation products over the three poles. *Int. J. Appl. Earth Obs. Geoinf.* **2021**, *104*, 102538. [CrossRef]
6. Gui, S.; Liang, S.; Li, L. Evaluation of satellite-estimated surface longwave radiation using ground-based observations. *J. Geophys. Res. Atmos.* **2010**, *115*, D18214. [CrossRef]
7. King, M.D.; Platnick, S.; Menzel, W.P.; Ackerman, S.A.; Hubanks, P.A. Spatial and Temporal Distribution of Clouds Observed by MODIS Onboard the Terra and Aqua Satellites. *IEEE Trans. Geosci. Remote Sens.* **2013**, *51*, 3826–3852. [CrossRef]
8. Matus, A.V.; L'Ecuyer, T.S. The role of cloud phase in Earth's radiation budget. *J. Geophys. Res. Atmos.* **2017**, *122*, 2559–2578. [CrossRef]
9. Liu, M.; Zheng, X.; Zhang, J.; Xia, X. A revisiting of the parametrization of downward longwave radiation in summer over the Tibetan Plateau based on high-temporal-resolution measurements. *Atmos. Chem. Phys.* **2020**, *20*, 4415–4426. [CrossRef]
10. Zhong, L.; Zou, M.; Ma, Y.; Huang, Z.; Xu, K.; Wang, X.; Ge, N.; Cheng, M. Estimation of Downwelling Shortwave and Longwave Radiation in the Tibetan Plateau Under All-Sky Conditions. *J. Geophys. Res. Atmos.* **2019**, *124*, 11086–11102. [CrossRef]
11. Lopes, F.M.; Dutra, E.; Trigo, I.F. Integrating Reanalysis and Satellite Cloud Information to Estimate Surface Downward Long-Wave Radiation. *Remote Sens.* **2022**, *14*, 1704. [CrossRef]
12. Yang, F.; Cheng, J. A framework for estimating cloudy sky surface downward longwave radiation from the derived active and passive cloud property parameters. *Remote Sens. Environ.* **2020**, *248*, 111972. [CrossRef]

13. Wang, T.; Shi, J.; Yu, Y.; Husi, L.; Gao, B.; Zhou, W.; Ji, D.; Zhao, T.; Xiong, C.; Chen, L. Cloudy-sky land surface longwave downward radiation (LWDR) estimation by integrating MODIS and AIRS/AMSU measurements. *Remote Sens. Environ.* **2018**, *205*, 100–111. [CrossRef]
14. Zhou, Y.; Kratz, D.P.; Wilber, A.C.; Gupta, S.K.; Cess, R.D. An improved algorithm for retrieving surface downwelling longwave radiation from satellite measurements. *J. Geophys. Res. Atmos.* **2007**, *112*, D15102. [CrossRef]
15. Zeng, Q.; Cheng, J.; Dong, L. Assessment of the Long-Term High-Spatial-Resolution Global LAnd Surface Satellite (GLASS) Surface Longwave Radiation Product Using Ground Measurements. *IEEE J-STARS* **2020**, *13*, 2032–2055. [CrossRef]
16. Duan, S.-B.; Han, X.-J.; Huang, C.; Li, Z.-L.; Wu, H.; Qian, Y.; Gao, M.; Leng, P. Land Surface Temperature Retrieval from Passive Microwave Satellite Observations: State-of-the-Art and Future Directions. *Remote Sens.* **2020**, *12*, 2573. [CrossRef]
17. Alsweiss, S.O.; Jelenak, Z.; Chang, P.S. Remote Sensing of Sea Surface Temperature Using AMSR-2 Measurements. *IEEE J-STARS* **2017**, *10*, 3948–3954. [CrossRef]
18. Prakash, S.; Norouzi, H.; Azarderakhsh, M.; Blake, R.; Prigent, C.; Khanbilvardi, R. Estimation of Consistent Global Microwave Land Surface Emissivity from AMSR-E and AMSR2 Observations. *J. Appl. Meteorol. Climatol.* **2018**, *57*, 907–919. [CrossRef]
19. Li, X.; Wigneron, J.-P.; Fan, L.; Frappart, F.; Yueh, S.H.; Colliander, A.; Ebtehaj, A.; Gao, L.; Fernandez-Moran, R.; Liu, X.; et al. A new SMAP soil moisture and vegetation optical depth product (SMAP-IB): Algorithm, assessment and inter-comparison. *Remote Sens. Environ.* **2022**, *271*, 112921. [CrossRef]
20. Wang, M.; Wigneron, J.-P.; Sun, R.; Fan, L.; Frappart, F.; Tao, S.; Chai, L.; Li, X.; Liu, X.; Ma, H.; et al. A consistent record of vegetation optical depth retrieved from the AMSR-E and AMSR2 X-band observations. *Int. J. Appl. Earth Obs. Geoinf.* **2021**, *105*, 102609. [CrossRef]
21. Derin, Y.; Bhuiyan, M.A.E.; Anagnostou, E.; Kalogiros, J.; Anagnostou, M.N. Modeling Level 2 Passive Microwave Precipitation Retrieval Error Over Complex Terrain Using a Nonparametric Statistical Technique. *IEEE Trans. Geosci. Remote Sens.* **2021**, *59*, 9021–9032. [CrossRef]
22. O'Dell, C.W.; Wentz, F.J.; Bennartz, R. Cloud Liquid Water Path from Satellite-Based Passive Microwave Observations: A New Climatology over the Global Oceans. *J. Clim.* **2008**, *21*, 1721–1739. [CrossRef]
23. Ji, D.; Shi, J.; Xiong, C.; Wang, T.; Zhang, Y. A total precipitable water retrieval method over land using the combination of passive microwave and optical remote sensing. *Remote Sens. Environ.* **2017**, *191*, 313–327. [CrossRef]
24. Li, Z.-L.; Tang, B.-H.; Wu, H.; Ren, H.; Yan, G.; Wan, Z.; Trigo, I.F.; Sobrino, J.A. Satellite-derived land surface temperature: Current status and perspectives. *Remote Sens. Environ.* **2013**, *131*, 14–37. [CrossRef]
25. Jiao, Z.-H.; Mu, X. Global validation of clear-sky models for retrieving land-surface downward longwave radiation from MODIS data. *Remote Sens. Environ.* **2022**, *271*, 112903. [CrossRef]
26. Schlüssel, P.; Schanz, L.; Englisch, G. Retrieval of latent heat flux and longwave irradiance at the sea surface from SSM/I and AVHRR measurements. *Adv. Space Res.* **1995**, *16*, 107–116. [CrossRef]
27. Liu, Q.; Simmer, C.; Ruprecht, E. Estimating Longwave Net Radiation at Sea Surface from the Special Sensor Microwave/Imager (SSM/I). *J. Appl. Meteorol.* **1997**, *36*, 919–930. [CrossRef]
28. Maeda, T.; Taniguchi, Y.; Imaoka, K. GCOM-W1 AMSR2 Level 1R Product: Dataset of Brightness Temperature Modified Using the Antenna Pattern Matching Technique. *IEEE Trans. Geosci. Remote Sens.* **2016**, *54*, 770–782. [CrossRef]
29. Hersbach, H.; Bell, B.; Berrisford, P.; Hirahara, S.; Horányi, A.; Muñoz-Sabater, J.; Nicolas, J.; Peubey, C.; Radu, R.; Schepers, D.; et al. The ERA5 global reanalysis. *Q. J. Roy. Meteorol. Soc.* **2020**, *146*, 1999–2049. [CrossRef]
30. Saunders, R.; Hocking, J.; Turner, E.; Rayer, P.; Rundle, D.; Brunel, P.; Vidot, J.; Roquet, P.; Matricardi, M.; Geer, A.; et al. An update on the RTTOV fast radiative transfer model (currently at version 12). *Geosci. Model Dev.* **2018**, *11*, 2717–2737. [CrossRef]
31. Feng, C.; Zhang, X.; Xu, J.; Yang, S.; Guan, S.; Jia, K.; Yao, Y. Comprehensive assessment of global atmospheric downward longwave radiation in the state-of-the-art reanalysis using satellite and flux tower observations. *Clim. Dyn.* **2022**. [CrossRef]
32. Tang, W.; Qin, J.; Yang, K.; Zhu, F.; Zhou, X. Does ERA5 outperform satellite products in estimating atmospheric downward longwave radiation at the surface? *Atmos. Res.* **2021**, *252*, 105453. [CrossRef]
33. Driemel, A.; Augustine, J.; Behrens, K.; Colle, S.; Cox, C.; Cuevas-Agulló, E.; Denn, F.M.; Duprat, T.; Fukuda, M.; Grobe, H.; et al. Baseline Surface Radiation Network (BSRN): Structure and data description (1992–2017). *Earth Syst. Sci. Data.* **2018**, *10*, 1491–1501. [CrossRef]
34. Ohmura, A.; Gilgen, H.; Hegner, H.; Müller, G.; Wild, M.; Dutton, E.G.; Forgan, B.; Fröhlich, C.; Philipona, R.; Heimo, A.; et al. Baseline Surface Radiation Network (BSRN/WCRP): New Precision Radiometry for Climate Research. *Bull. Am. Meteorol. Soc.* **1998**, *79*, 2115–2136. [CrossRef]
35. Liang, S.L.; Wang, K.C.; Zhang, X.T.; Wild, M. Review on Estimation of Land Surface Radiation and Energy Budgets From Ground Measurement, Remote Sensing and Model Simulations. *IEEE J-STARS* **2010**, *3*, 225–240. [CrossRef]
36. McPhaden, M.J.; Meyers, G.; Ando, K.; Masumoto, Y.; Murty, V.S.N.; Ravichandran, M.; Syamsudin, F.; Vialard, J.; Yu, L.; Yu, W. RAMA: The Research Moored Array for African–Asian–Australian Monsoon Analysis and Prediction. *Bull. Am. Meteorol. Soc.* **2009**, *90*, 459–480. [CrossRef]
37. McPhaden, M.; Busalacchi, A.; Anderson, D. A TOGA Retrospective. *Oceanography* **2010**, *23*, 86–103. [CrossRef]
38. Schmetz, J. Towards a surface radiation climatology: Retrieval of downward irradiances from satellites. *Atmos. Res.* **1989**, *23*, 287–321. [CrossRef]

39. Parinussa, R.M.; Holmes, T.R.H.; Yilmaz, M.T.; Crow, W.T. The impact of land surface temperature on soil moisture anomaly detection from passive microwave observations. *Hydrol. Earth Syst. Sci.* **2011**, *15*, 3135–3151. [CrossRef]
40. Wu, Y.; Qian, B.; Bao, Y.; Li, M.; Petropoulos, G.P.; Liu, X.; Li, L. Detection and Analysis of C-Band Radio Frequency Interference in AMSR2 Data over Land. *Remote Sens.* **2019**, *11*, 1228. [CrossRef]
41. Chen, T.; Guestrin, C. XGBoost: A Scalable Tree Boosting System. In Proceedings of the 22nd ACM SIGKDD International Conference on Knowledge Discovery and Data Mining, San Francisco, CA, USA, 13–17 August 2016; pp. 785–794.
42. Lundberg, S.M.; Erion, G.; Chen, H.; DeGrave, A.; Prutkin, J.M.; Nair, B.; Katz, R.; Himmelfarb, J.; Bansal, N.; Lee, S.I. From Local Explanations to Global Understanding with Explainable AI for Trees. *Nat. Mach. Intell.* **2020**, *2*, 56–67. [CrossRef] [PubMed]
43. Reichstein, M.; Camps-Valls, G.; Stevens, B.; Jung, M.; Denzler, J.; Carvalhais, N. Deep learning and process understanding for data-driven Earth system science. *Nature* **2019**, *566*, 195–204. [CrossRef] [PubMed]
44. Ge, Y.; Zhang, X.; Atkinson, P.M.; Stein, A.; Li, L. Geoscience-aware deep learning: A new paradigm for remote sensing. *Sci. Remote Sens.* **2022**, *5*, 100047. [CrossRef]
45. Jiao, Z.-H.; Mu, X. Single-footprint retrieval of clear-sky surface longwave radiation from hyperspectral AIRS data. *Int. J. Appl. Earth Obs. Geoinf.* **2022**, *110*, 102802. [CrossRef]
46. Kratz, D.P.; Gupta, S.K.; Wilber, A.C.; Sothcott, V.E. Validation of the CERES Edition-4A Surface-Only Flux Algorithms. *J. Appl. Meteorol. Climatol.* **2020**, *59*, 281–295. [CrossRef]
47. Morcrette, J.-J. The surface downward longwave radiation in the ECMWF forecast system. *J. Clim.* **2002**, *15*, 1875–1892. [CrossRef]
48. Mao, K.; Shi, J.; Li, Z.; Qin, Z.; Li, M.; Xu, B. A physics-based statistical algorithm for retrieving land surface temperature from AMSR-E passive microwave data. *Sci. China Ser. D-Earth Sci.* **2007**, *50*, 1115–1120. [CrossRef]
49. Huang, C.; Duan, S.-B.; Jiang, X.-G.; Han, X.-J.; Leng, P.; Gao, M.-F.; Li, Z.-L. A physically based algorithm for retrieving land surface temperature under cloudy conditions from AMSR2 passive microwave measurements. *Int. J. Remote Sens.* **2018**, *40*, 1828–1843. [CrossRef]
50. Holmes, T.R.H.; De Jeu, R.A.M.; Owe, M.; Dolman, A.J. Land surface temperature from Ka band (37 GHz) passive microwave observations. *J. Geophys. Res. Atmos.* **2009**, *114*, D04113. [CrossRef]
51. Ninghai, S.; Fuzhong, W. Evaluation of Special Sensor Microwave Imager/Sounder (SSMIS) Environmental Data Records. *IEEE Trans. Geosci. Remote Sens.* **2008**, *46*, 1006–1016. [CrossRef]
52. Bonafoni, S.; Mattioli, V.; Basili, P.; Ciotti, P.; Pierdicca, N. Satellite-Based Retrieval of Precipitable Water Vapor Over Land by Using a Neural Network Approach. *IEEE Trans. Geosci. Remote Sens.* **2011**, *49*, 3236–3248. [CrossRef]
53. Schmeisser, L.; Hinkelman, L.M.; Ackerman, T.P. Evaluation of Radiation and Clouds From Five Reanalysis Products in the Northeast Pacific Ocean. *J. Geophys. Res. Atmos.* **2018**, *123*, 7238–7253. [CrossRef]
54. Lenaerts, J.T.M.; Van Tricht, K.; Lhermitte, S.; L'Ecuyer, T.S. Polar clouds and radiation in satellite observations, reanalyses, and climate models. *Geophys. Res. Lett.* **2017**, *44*, 3355–3364. [CrossRef]
55. de Nijs, A.H.A.; Parinussa, R.M.; de Jeu, R.A.M.; Schellekens, J.; Holmes, T.R.H. A Methodology to Determine Radio-Frequency Interference in AMSR2 Observations. *IEEE Trans. Geosci. Remote Sens.* **2015**, *53*, 5148–5159. [CrossRef]
56. Eytan, E.; Koren, I.; Altaratz, O.; Kostinski, A.B.; Ronen, A. Longwave radiative effect of the cloud twilight zone. *Nat. Geosci.* **2020**, *13*, 669–673. [CrossRef]
57. Muñoz-Sabater, J.; Dutra, E.; Agustí-Panareda, A.; Albergel, C.; Arduini, G.; Balsamo, G.; Boussetta, S.; Choulga, M.; Harrigan, S.; Hersbach, H.; et al. ERA5-Land: A state-of-the-art global reanalysis dataset for land applications. *Earth Syst. Sci. Data* **2021**, *13*, 4349–4383. [CrossRef]
58. van der Schalie, R.; van der Vliet, M.; Albergel, C.; Dorigo, W.; Wolski, P.; de Jeu, R. Characterizing natural variability in complex hydrological systems using passive microwave-based climate data records: A case study for the Okavango Delta. *Hydrol. Earth Syst. Sci.* **2022**, *26*, 3611–3627. [CrossRef]
59. Wang, T.; Zeng, J.; Chen, K.-S.; Li, Z.; Ma, H.; Chen, Q.; Bi, H.; Shi, P.; Zhu, L.; Cui, C. Comparison of Different Intercalibration Methods of Brightness Temperatures From FY-3D and AMSR2. *IEEE Trans. Geosci. Remote Sens.* **2022**, *60*, 1–17. [CrossRef]
60. Wu, P.; Su, Y.; Duan, S.-b.; Li, X.; Yang, H.; Zeng, C.; Ma, X.; Wu, Y.; Shen, H. A two-step deep learning framework for mapping gapless all-weather land surface temperature using thermal infrared and passive microwave data. *Remote Sens. Environ.* **2022**, *277*, 113070. [CrossRef]
61. Cucchi, M.; Weedon, G.P.; Amici, A.; Bellouin, N.; Lange, S.; Müller Schmied, H.; Hersbach, H.; Buontempo, C. WFDE5: Bias-adjusted ERA5 reanalysis data for impact studies. *Earth Syst. Sci. Data* **2020**, *12*, 2097–2120. [CrossRef]